applied sciences

MDPI

Article

Bidirectional Fluid–Structure Interaction Study on Hydrofoil Hardness and Oscillation Mode Optimization

Ertian Hua, Mingwang Xiang *, Qizong Sun, Tao Wang, Yabo Song and Caiju Lu

College of Mechanical Engineering, Zhejiang University of Technology, Hangzhou 310023, China; het@zjut.edu.cn (E.H.); 121222020046@zjut.edu.cn (Q.S.); 221122020431@zjut.edu.cn (T.W.); 221122020206@zjut.edu.cn (Y.S.); 221122020367@zjut.edu.cn (C.L.)

* Correspondence: 211122020035@zjut.edu.cn; Tel.: +86-15-86-858-8517

Featured Application: This paper focuses on the optimization of the application parameters of ultra-low-head bionic hydrofoil devices under low head conditions in the plain's river network region, aiming to improve the self-purification capability of small ecological water bodies with slow water flow and very small water level differences, such as urban small channels, fishery runway aquaculture systems, and man-made open channels. The existing ultra-low head bionic hydrofoil device is based on the symmetric hydrofoil design of NACA0012 with a fish-tail-like structure, which realizes highly efficient pumping work under low-frequency conditions by the coupled movement of heaving and pitching two-degrees-of-freedom. To enhance the performance of this device in practical engineering, this research adopted a bidirectional fluid–structure coupling method, systematically analyzed the influence of hydrofoil hardness and frequency on its hydrodynamic performance, and found the optimal hydrofoil hardness and the optimal swinging mode of the flexible hydrofoil. The results showed that through the optimization of these parameters, a more efficient pumping effect can be achieved under low flow and low head conditions, while maintaining the friendliness to aquatic organisms. This optimization scheme provides further technical support for the practical application of ultra-low head bionic hydrofoils in plain river network areas, which helps to solve the water pollution problem caused by insufficient hydrodynamic force at low head.

Abstract: This paper investigated the optimization of the hardness and oscillation mode of flexible hydrofoils using bidirectional fluid–structure interaction (FSI) to address the issue of insufficient guidance in engineering applications. A two-dimensional flexible symmetric hydrofoil model of NACA0012 with a chord length of 1 m was constructed for this research. The hydrodynamic characteristics of low-frequency flexible hydrofoils with varying hardness and oscillation modes were analyzed through numerical simulation. The results indicated that the flexible hydrofoil with a Shore hardness of D50 exhibited the most optimal hydrodynamic performance under low-frequency conditions across the five groups of hardness tests. Among the three commonly utilized oscillation modes, the inboard oscillation mode demonstrated the most favorable performance. The hydrodynamic performance of the flexible hydrofoil surpassed that of the rigid hydrofoil in both inward and outward oscillation motions; however, it was inferior in pure pitching motions. Comparative analysis of the vortex structure and velocity distribution in the flow field revealed that the inward oscillation motion effectively enhanced the kinetic energy of the wake vortex and slowed down vortex dissipation, thereby improving the overall flow velocity. These findings provide theoretical support for the study of flexible hydrofoils and contribute to their advancement in pumping applications under actual ultra-low head conditions.

Academic Editor: Junhong Park

Received: 10 December 2024
Revised: 9 January 2025
Accepted: 15 January 2025
Published: 16 January 2025

Citation: Hua, E.; Xiang, M.; Sun, Q.; Wang, T.; Song, Y.; Lu, C. Bidirectional Fluid–Structure Interaction Study on Hydrofoil Hardness and Oscillation Mode Optimization. *Appl. Sci.* **2025**, *15*, 825. https://doi.org/10.3390/app15020825

Keywords: flexible hydrofoil; Shore hardness of the hydrofoil; bidirectional fluid–structure interaction; oscillation mode; hydrodynamic performance

1. Introduction

In the low-lying plains and river network areas of the southern China, insufficient hydraulic dynamics in ecological water bodies pose a widespread challenge [1]. Previous studies have shown that low-head axial flow pumps perform inadequately in practical applications [2]. Feng et al. [3] demonstrated that hydrofoils, which mimic the movement of fish, offer several advantages, including low resistance, high maneuverability, low noise, and a suitability for ultra-low head conditions. These properties make hydrofoils particularly significant for enhancing the hydraulic dynamics of ecological water bodies under ultra-low head conditions in plain areas. Despite these benefits, hydrofoils have not been widely adopted as a pumping strategy, primarily due to the lack of comprehensive theoretical research on their hydrodynamic behavior.

The earliest research on hydrofoils was mainly based on the aerodynamic transformation of airfoils. Scholars combined the aerodynamic advantages of airfoils with the swimming mechanism of fish and obtained the hydrofoil device through the active oscillatory movement of the airfoil wing shape in the water. The pumping mechanism of a hydrofoil is the formation of reversed Kármán vortex streets by the shedding of trailing edge vortex pairs, which in turn generates a jet. To further optimize the hydrodynamic performance of the hydrofoil, scholars have conducted extensive research on the hydrofoil parameters. Du et al. [4] employed numerical methods to simulate and analyze the water propulsion effects of four different hydrofoil motion modes, thereby identifying the optimal motion modes of the hydrofoil. Ding et al. [5] integrated the underwater motion model of the hydrofoil with the method of thrust efficiency estimation, analyzed the numerical results of the propulsive performance under various motion conditions, and determined the optimal thrust. The optimal efficiency points for the lifting-and-pitching amplitude and frequency of the rigid hydrofoil were determined. An overlapping grid strategy was employed by Li et al. [6] to numerically simulate a hydrofoil, with consideration given to wall effects. Based on the analysis of the flow mechanism, the optimal wall spacing for achieving maximum propulsive efficiency was determined to be 0.8c (where c is the hydrofoil chord length).

In research on stiffer hydrofoils, scholars have assumed the hydrofoils to be rigid models. This assumption has had the effect of neglecting the deformation caused by forces during the study of their hydrodynamic characteristics. As a result, the complexity of hydrofoil research is simplified. However, when hydrofoils are in motion, they inevitably deform due to the reactive forces from the fluid. This deformation is not only dependent on the hardness of the hydrofoil but is also influenced by factors such as oscillation frequency and the Reynolds number. By ignoring this aspect, the rigid model introduces a certain degree of computational error. This inaccuracy is magnified when investigating flexible hydrofoils with large deformations and therefore cannot be simplified to a rigid model.

Flexible hydrofoils demonstrate markedly enhanced hydrodynamic performance under specific conditions when compared to rigid hydrofoils. YG Ryu et al. [7] employed Digital Particle Image Velocity (DPIV) to quantify the aerodynamic forces, torque, and flow vector fields of both rigid and flexible foils equipped with leading-edge veins. Their findings revealed that minimal foil surface deformation not only reduces the distance between vortices and the foil surface but also delays vortex dispersion, enhances foil flow intensity, and thus generates a higher initial peak lift. This suggests that within a specific

range of chord-wise flexibility, flexible foils exhibit enhanced efficiency. Furthermore, Liu et al. [8] demonstrated through numerical simulations that the flexible deformation of hydrofoils contributes to increased vortex strength and reduced energy dissipation, thereby enhancing propulsion performance. Additionally, the role of flexibility in enabling energy-efficient movement has drawn increasing attention, inspired by natural swimmers such as fish and birds, which utilize intermittent movements to maximize thrust efficiency and minimize energy consumption. Zhou et al. [9] investigated the hydrodynamic performance of a bionic tail fin and found that spreading flexibility can increase thrust and maintain high propulsive efficiency. As a result, flexible hydrofoils represent an important area of research, but many research deficiencies and gaps remain. Some recent studies have referred to the flexible deformation of hovering airfoils and proposed the use of active flexibility to replace passive deformation in hydrofoils [10]. However, this approach does not consider the coupling force exerted by the fluid during hydrofoil motion and has some limitations. In contrast, the bidirectional fluid–structure interaction method employed in this study enables real-time feedback between fluid forces and structural deformation. This approach provided a more comprehensive and accurate simulation of the complex mechanical interactions of flexible hydrofoils in dynamic fluid environments, overcoming the limitations of unidirectional coupling models and improving computational precision.

The research conducted by Gao et al. [11] indicated that flexible hydrofoils can generate superior thrust compared to their rigid counterparts at a low frequency of 1 Hz. However, alterations in the hardness of the hydrofoil will unavoidably result in fluctuations in deformation, and the hydrodynamic performance of hydrofoils constructed from disparate materials will also diverge. Furthermore, during actual motion, flexible hydrofoils will deform in varying ways contingent on the motion way employed. Therefore, this study focused on analyzing the effects of Shore hardness and motion modes, providing a basis for optimal design choices in practical applications. Furthermore, about the matter of model dimensions, Deng et al. [12] demonstrated that hydrofoils exhibit three-dimensional instability under a specific pitching amplitude through Floquet stability analysis. To circumvent the three-dimensional instability factor in the study of the impact of hydrofoil chord-wise flexibility on hydrodynamic performance, this paper employed a chord-wise two-dimensional model of the hydrofoil.

The central inquiry of this study pertained to the influence of Shore hardness and oscillation mode on the hydrodynamic performance of flexible hydrofoils under ultra-low head conditions. The objective of this study was to enhance the comprehension of the passive deformation characteristics of flexible hydrofoils and their application in the context of water flow dynamics in ecological water bodies. To this end, a two-dimensional model of flexible hydrofoils was constructed, and the chord-wise deformation behavior of hydrofoils was simulated under different conditions. This was achieved by applying a coupling force based on the bidirectional fluid–structure interaction technique. The differences in hydrodynamic characteristics between flexible hydrofoils and rigid hydrofoils were analyzed, and the hydrodynamic characteristics of flexible hydrofoils with varying chord-wise deformations were compared with those of flexible hydrofoils with different low-frequency motions. The grid and time-step independence of the model were verified, thereby improving the accuracy and reliability of the model. The viability of the simulation approach was validated by comparing the results with the experimental data from existing studies. Subsequently, the optimal hardness of the flexible hydrofoil was determined by considering the pumping efficiency and propulsion efficiency as evaluation criteria. Additionally, the hydrodynamic characteristics of the flexible hydrofoil under different motion methods at low frequency (1 Hz) were compared, which provides a reference for the research of hydrofoil devices.

This study contributes significantly to advancing the design of flexible hydrofoils by offering practical solutions for real-world applications. The flexible hydrofoils analyzed in this paper are particularly suitable for small-scale hydraulic applications such as improving water circulation in plain river networks, the power optimization of marine probes, pollutant discharge in aquaculture circuits, and pumping in low-head channels. The optimized flexible hydrofoils are more adaptable and ecologically compatible, providing a promising solution to cope with the conditions. Although the proposed solution shows potential in enhancing hydrodynamic performance under ultra-low head conditions, this study does not include a direct comparison of energy consumption between the flexible hydrofoil and traditional pumps or mixers. Future work could incorporate detailed energy efficiency analyses to further validate the benefits of the proposed system.

Furthermore, the dimensionless numbers (Reynolds number and Strouhal number) that are required for the defining study are presented in Equations (1) and (2).

$$\mathrm{Re} = \frac{\rho \overline{U} c}{\mu}, \tag{1}$$

$$St = \frac{f h_{\max}}{\overline{U}}, \tag{2}$$

where ρ = 998.2 kg/m^3 is the density of water at room temperature at 293.15 K; $\overline{U}$ is the average incoming velocity, where the average incoming velocity generated by the hydrofoil device in this paper was 0.3 m/s; c is the chord length of the hydrofoil, which was taken to be 1 m in this paper; μ = 1.005 $\times$ 10^{-3} Pa·m^2 is the coefficient of the hydrodynamic viscosity of water at room temperature; f is the frequency; and h_{max} is the amplitude of the lifting, which was taken to be half of the chord length (0.5c).

2. Methods

In this section, we first introduce the basic physical models adopted in this study, including the hydrofoil structure and motion model as well as the flow channel model. Subsequently, the mathematical models utilized in this paper are presented, encompassing kinematic and dynamic parameters, the bidirectional fluid–structure interaction process, the numerical model of the fluid domain, and the structural dynamics model of the solid domain. Lastly, the solution strategy and method validation employed in this work are detailed, including boundary conditions and mesh division, mesh independence verification, and validation of the fluid–structure interaction method. This provided a reliable model and fundamental theoretical basis for the subsequent research.

2.1. Physical Models

Most extant research on hydrofoils has elected to utilize the NACA series of airfoils, developed by the National Advisory Committee for Aeronautics (NACA), as the research model. In this paper, the NACA0012 two-dimensional flexible symmetric airfoil with a chord length of c = 1 m was employed as a case study. By conducting transient calculations on the flexible deformation of the 2D hydrofoil, it was possible to compare the chord-wise deformation of the hydrofoil under different motion positions. This approach avoided the interference of spreading deformation and was more aligned with the research requirements. In the numerical simulation, the dimensionless structure of the hydrofoil is illustrated in Figure 1. The thickness was 0.12 m, and the pivot position was 0.2c.

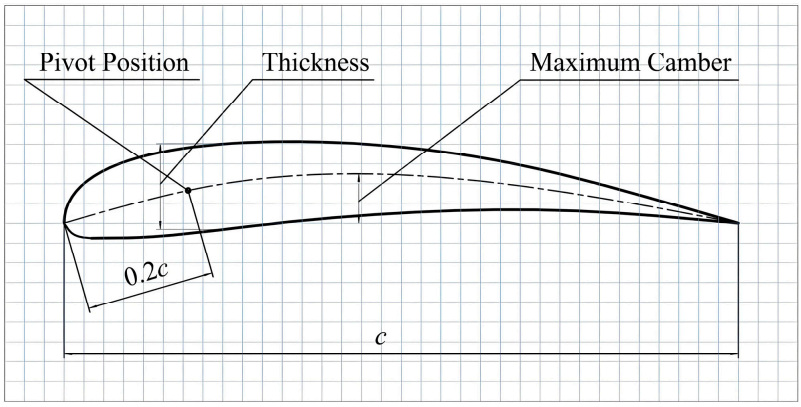

Figure 1. Schematic diagram of the NACA0012 flexible hydrofoil structure.

The motion of the hydrofoil coupled two ways of pitching and lifting, and the basic equations of motion are as follows:

$$\begin{cases} h(t) = h_{\max} sin(2\pi ft + \varphi_h) \\ \theta(t) = \theta_{\max} sin(2\pi ft + \varphi_\theta) \end{cases}, \quad (3)$$

where $\theta_{\max}$ is the pitching amplitude, which was taken as $\pi/6$ rad; φ_h is the heaving phase difference; φ_θ is the pitching phase difference; and f is the frequency of hydrofoil motion, and in practical applications, too high a motion frequency will lead to overloading of the hydrofoil drive mechanism, so in order to ensure the reasonableness of the practical application of hydrofoils, the frequency in this paper was set at 0.5 Hz. According to the above basic equations of motion, three motion ways were obtained as shown in Figure 2. For the inward oscillation motion way, h_{max} = 0.5c, $\varphi_h = 3\pi/2$, and $\varphi_\theta = \pi$; for the outward oscillation motion way, h_{max} = 0.5c, φ_h = 0, and φ_θ = 0; and for the pitch-only oscillation motion way, h_{max} = 0, φ_h = 0, and φ_θ = 0.

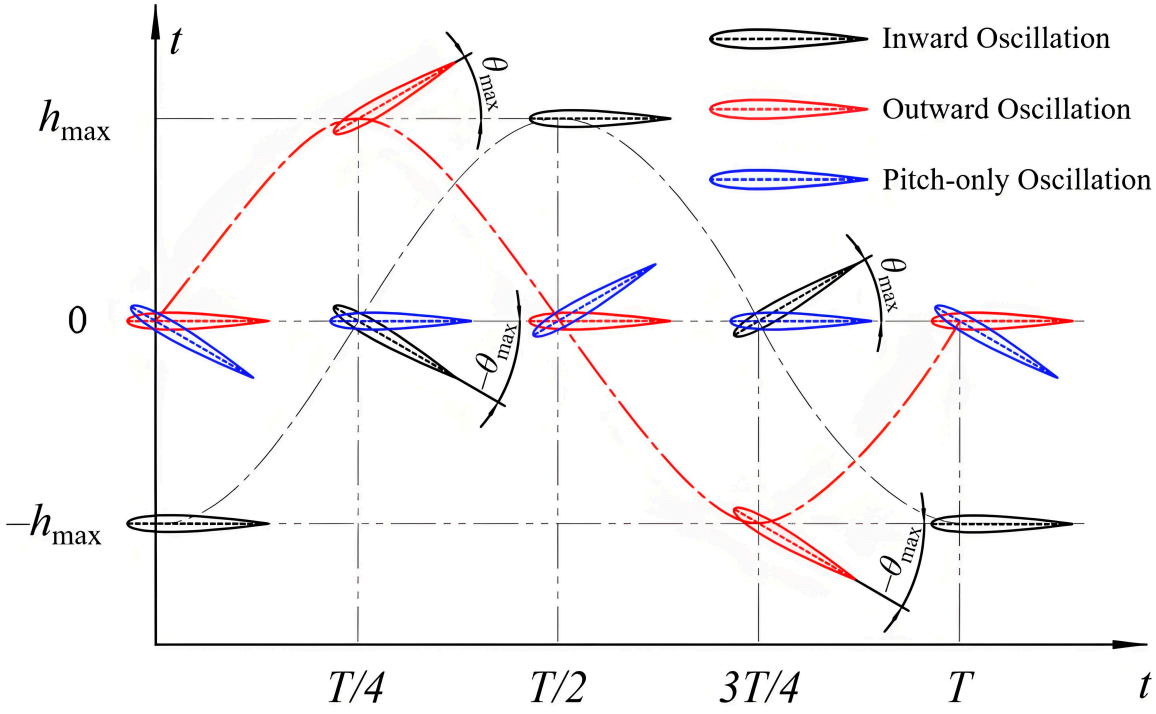

Figure 2. Schematic diagram of the heaving and pitching motion.

The two-dimensional flow channel model of the hydrofoil is shown in Figure 3, as proposed by Li et al. [6]; the optimal hydrodynamic performance of the hydrofoil can be achieved by setting the width of the flow channel to 0.8c. However, in this paper, the maximum distance in the y-direction of the hydrofoil increased by an additional $2c{\cdot}\sin\theta_{\max}$ meters when the hydrofoil was moving in an outward pendulum motion. Accordingly, the width of the flow channel was calibrated in accordance with the ratio, with the objective of preventing hydrofoil displacement and wall-related interference. The selected flow channel width was 2.8 m. Furthermore, the distance between the hydrofoil and the flow channel inlet was set to 3 m to gain a more comprehensive understanding of the evolution of the flow field. To gain a more detailed observation of the vortices generated by the hydrofoil motion, it was necessary to ensure that the distance between the hydrofoil and the flow channel outlet was sufficient for the reversed Kármán vortex street to dissipate and generate a relatively uniform velocity field. Therefore, the total length of the flow channel was set to 15 m.

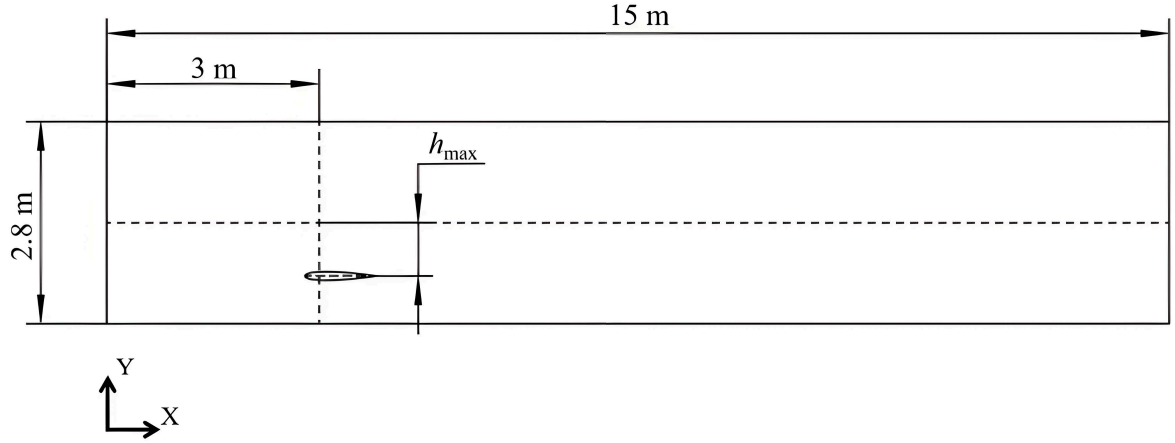

Figure 3. Schematic diagram of the flow channel.

2.2. Evaluation Parameters and Numerical Modeling

2.2.1. Kinematic Parameters and Mechanical Parameters

In the hydrodynamic performance study of hydrofoil, the mean thrust coefficient $\overline{C}_t$ and mean lift coefficient $\overline{C}_y$ can effectively represent the force of the hydrofoil, which is a key parameter to measure the hydrodynamic performance of the hydrofoil; the formulas for calculating the mean thrust coefficient $\overline{C}_t$ and mean lift coefficient $\overline{C}_y$ are as follows [13]:

$$\mathbf{C_p} = \frac{1}{kT}\int_{(n-k)T}^{nT} \mathbf{C_s} dt, \tag{4}$$

where $\mathbf{C_p}$ is the average force coefficient matrix, $\mathbf{C_p} = [\overline{C}_t, \overline{C}_y]^T$; $\mathbf{C_s}$ is the instantaneous force coefficient matrix, $\mathbf{C_s} = [\mathrm{C_t}(t), \mathrm{C_y}(t)]^{\mathrm{T}}$; n is the total number of oscillation cycles of the calculation; k is the number of oscillation cycles, taken as 1; $\mathrm{C}_t(t)$ is the instantaneous lift coefficient, and the calculation formula is as follows:

$$\mathbf{C_s} = \mathbf{F_s} \cdot \frac{2}{\rho \overline{U}^2 cs}, \tag{5}$$

where $\mathbf{F_s}$ is the instantaneous thrust matrix. $\mathbf{F_s} = [F_x(t), F_y(t)]$ where $F_x(t)$ is the instantaneous thrust in the horizontal direction, N; F_y(t) is the instantaneous lift in the vertical direction, N; and s is the spreading length of the hydrofoil, which was taken to be 1 m by default for the two-dimensional calculations in this paper.

Furthermore, the propulsion efficiency η_{pt} and pumping efficiency η_{pb} are frequently employed in the domain of pumping research to assess the efficacy of hydrofoils. The underlying mathematical relationship can be expressed as follows:

$$\begin{cases} \eta_{pt} = \frac{\overline{F}_T \cdot \overline{U}}{\overline{P}_{in}} \\ \eta_{pb} = \frac{\Delta \overline{P} \cdot \overline{Q}}{\overline{P}_{in}} \end{cases}, \tag{6}$$

where $\Delta\overline{P}$ is the average pressure difference between the outlet and inlet of the flow channel; $\overline{F}_T$ is the average thrust generated by the hydrofoil on the fluid; $\overline{Q}$ is the average flow rate at the outlet; and $\overline{P}_{in}$ is the average input power; $\overline{F}_T$, $\overline{Q}$ and $\overline{P}_{in}$ are calculated as shown in Equations (7)–(9):

$$\overline{F}_T = \frac{1}{kT}\int_{(n-k)T}^{nT} F_x(t)dt, \tag{7}$$

$$\overline{Q} = \overline{U}bS, \tag{8}$$

$$\overline{P}_{in} = \frac{1}{T}\left(\left|\int_t^{t+T} F_y(t)\dot{h}(t)dt\right| + \left|\int_t^{t+T} M(t)\dot{\theta}(t)dt\right|\right), \tag{9}$$

where $M(t)$ is the instantaneous driving torque of the hydrofoil; T is the period time; $h(t)$ is the displacement in the Y-direction; $\theta(t)$ is the pitching angle; and b is the flow channel width, taken as 2.8 m.

2.2.2. Flexible Hydrofoil Fluid-Solid Coupling Process

Regarding the flexible deformation of hydrofoils, Wang et al. [10] investigated the effects of parameters such as the active flexible deformation mode, flexibility coefficient, and chord-wise deformation length on the propulsive characteristics of flexible hydrofoils by combining different forms of chord-wise deformation equations. Because in practical applications, active flexibility is usually used for hovering foils and is different from the actual hydrofoil motion. Therefore, in this paper, passive flexible deformation based on the bidirectional fluid–structure interaction technique was used. The deformation of the mesh was determined according to the transient structural force, as shown in Figure 4, which is a schematic diagram of the mesh in the fluid domain and the solid domain during the flexible deformation of the hydrofoil in this study, where D_d is the chord-wise deformation of the hydrofoil in m. The deformation of the hydrofoil when subjected to the fluid force was performed by the transient structural solver. The force on the hydrofoil in the transient structure solver was derived from the fluid domain solver, then the data were transferred to the fluid domain part through the system coupling, and finally the results were calculated to convergence through the coupled iteration method. In addition, since the bidirectional fluid–structure interaction method does not support calculation in a 2D plane, an extra thickness must be extended in the normal direction of the plane; but, in the meshing, a single layer boundary process was carried out in the direction of the thickness to avoid the extra 3D inaccuracy.

There are currently two main approaches to solving fluid–structure interaction (FSI) problems: monolithic coupling and partitioned iterative coupling. Monolithic coupling constructs coupled equations for both the fluid and solid domains and solves all variables simultaneously within a single time step. However, when the density ratio between the solid and fluid is large, this method requires a high-quality mesh. In contrast, partitioned iterative coupling offers more flexibility in terms of mesh quality requirements and is more widely used in FSI solutions. In partitioned iterative coupling, results are exchanged between the fluid and solid domains via interface coupling equations. Within a single time step, pressure data from the fluid solver are passed to the structural solver and then

displacement data from the solid solver are passed back to the fluid solver, achieving bi-directional FSI. This process is illustrated in Figure 5.

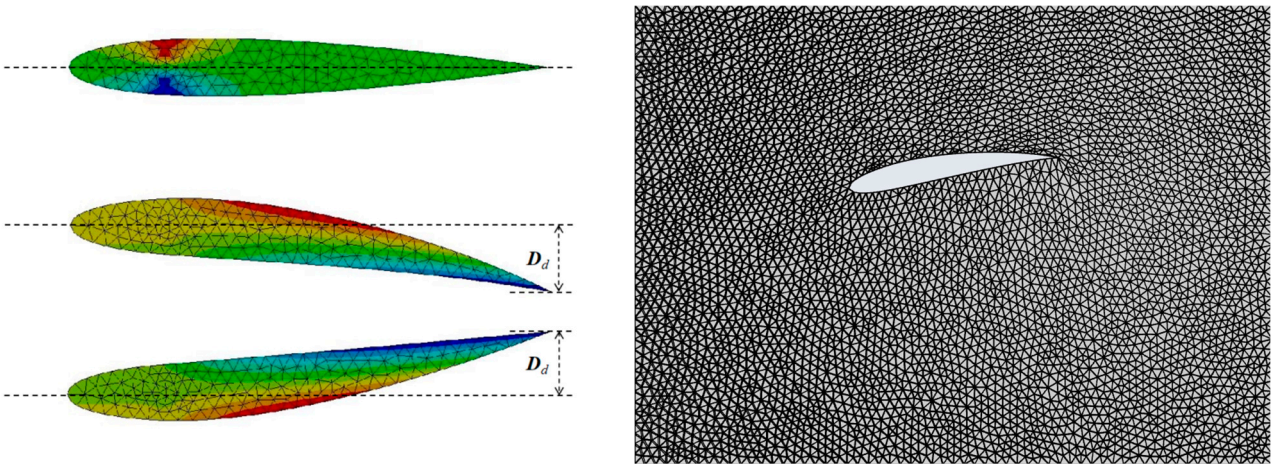

(**a**) (**b**)

Figure 4. Flexible hydrofoil grid deformation: (**a**) Solid domain mesh deformation; (**b**) Fluid domain mesh deformation.

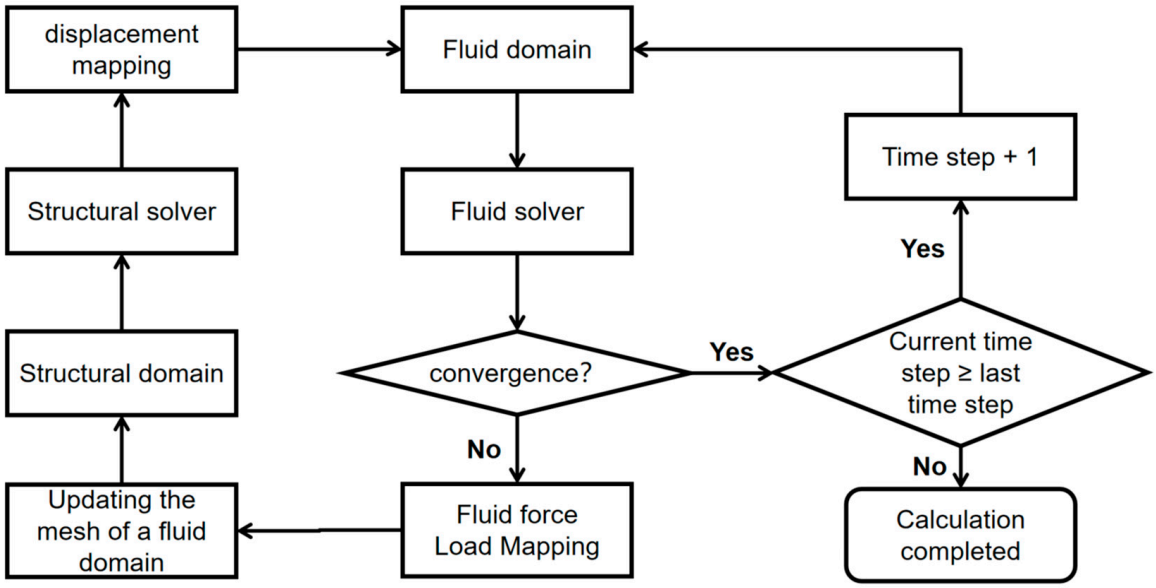

Figure 5. Partitioned iterative solution method flow.

2.2.3. Control Equations and Turbulence Modelling in Fluid Domains

The numerical calculations in this paper are divided into transient solutions in the fluid and solid domains. In the fluid domain computation, considering the computation as an in-compressible flow turbulence problem, the equations of motion control are the Reynolds-averaged Navier–Stokes (RANS) equations and the time-averaged continuity equations [14]:

$$\frac{\partial \overline{u}_i}{\partial x_i} = 0, \tag{10}$$

$$\frac{\partial v}{\partial t} + v \cdot \nabla v = -\frac{1}{\rho}\nabla \overline{p} + (\gamma + \gamma_t)\nabla^2 v \tag{11}$$

where $\overline{p}$ is the time-averaged pressure of the fluid, Pa. v is the average velocity of the fluid movement, m/s. γ is the laminar flow viscosity coefficient, Pa·s. γ_t is the turbulent flow viscosity coefficient, Pa·s.

Since the number of unknowns in the above system of equations is larger than the number of equations, a turbulence model was introduced to close the system of equations to find a definite solution. Commonly used turbulence models include the k-ω model and k-ε model, etc. The k-ε model is the most stable and widely used model among many turbulence models, which can improve the calculation speed while guaranteeing accuracy, so this paper chose the k-ε model in the numerical simulation. There are three kinds of k-ε models, namely, the standard k-ε model, the RNG k-ε model, and the realizable k-ε model. Since the fluid medium in this study was a viscous incompressible fluid, for the viscous problem, the realizable k-ε model adds an equation for the viscous term, which improved the accuracy and precision of the calculation results and was more in line with the computational needs of this paper. In summary, the realizable k-ε turbulence model was chosen to solve the N–S equations in this paper. The relevant equations can be found in a study by Shaheed et al. [14]. The utilization of bi-directional fluid–structure interactions to investigate the passive deformation of actively oscillating flexible hydrofoils is not a novel concept from the perspective of contemporary computational fluid dynamics (CFD) techniques. However, the present study contributed to the advancement of these methods by applying them to flexible hydrofoils under ultra-low head conditions. The integration of passive deformation analysis with Shore hardness and oscillation mode optimization under such conditions remains an under-explored area in the field. While the method itself is widely recognized in general CFD simulations, its application to solve the actual flexible deformation problem of oscillating hydrofoils is also of great importance in this field.

2.2.4. Structural Dynamics Modelling

In the solid domain, the structure of a hydrofoil changes with time due to the dynamic loads applied to the flexible hydrofoil during deformation. Therefore, transient dynamics analyses are required to consider the effects of inertia, damping, and dynamic loading at different moments. In this study, the following structural dynamics model was used for transient numerical iterations [15]:

$$\mathbf{M}\ddot{d} + \mathbf{Z}\dot{d} + \mathbf{K}d = \mathbf{F}_{\mathrm{FSI}} \tag{12}$$

where **M** is the structural force–mass matrix, consisting of the structural mass induced by the fluid inertial force, the static imbalance, and the rotational inertia. **Z** is the damping matrix, consisting of the structural damping values for the bending and torsional motions. **K** is the hardness matrix, consisting of the bending and torsional hardness values for the hydrofoil structure. d is the displacement vector, $d = [\boldsymbol{h}\ \boldsymbol{\theta}]^{\mathrm{T}}$. $\mathbf{F}_{\mathrm{FSI}}$ is the fluid–structure coupling force, which is synthesized by the variable load vector and the instantaneous force matrix.

2.3. Solution Strategy and Validation

2.3.1. Boundary Conditions and Meshing

In the CFD solution of fluid–structure coupling, the grid model needs to be divided, and boundary conditions are set. The hydrofoil boundary was set as the system coupling surface. Separate dynamic mesh regions in the hydrofoil region to minimize the number of mesh reconfigurations. According to Qi et al. [16] the time-varying free stream has less influence on the propulsive performance of a fully active oscillating hydrofoil, so the time-varying flow can be simplified to a certain extent into a steady flow field for numerical simulation. In this research, the inlet boundary was set as a pressure inlet, with the initial velocity at 0 m/s, and the outlet condition was set as a pressure outlet. In the grid division, the near-wall region was often divided into a viscous sub-layer, transition sub-layer, and a fully turbulent region from small to large according to the difference of

the dimensionless number (Y+) of the near-wall vortex computation. In this paper, the wall function of the realizable k-ε turbulence model was utilized to solve the near-wall region directly. Therefore, to better capture the characteristics of the fluid wall and prevent numerical dispersion, the first grid height of the wall boundary layer on both sides of the flow channel was set to 0.0001 m to achieve the requirement of Y+ < 1. The final fluid domain boundary conditions are shown in Figure 6.

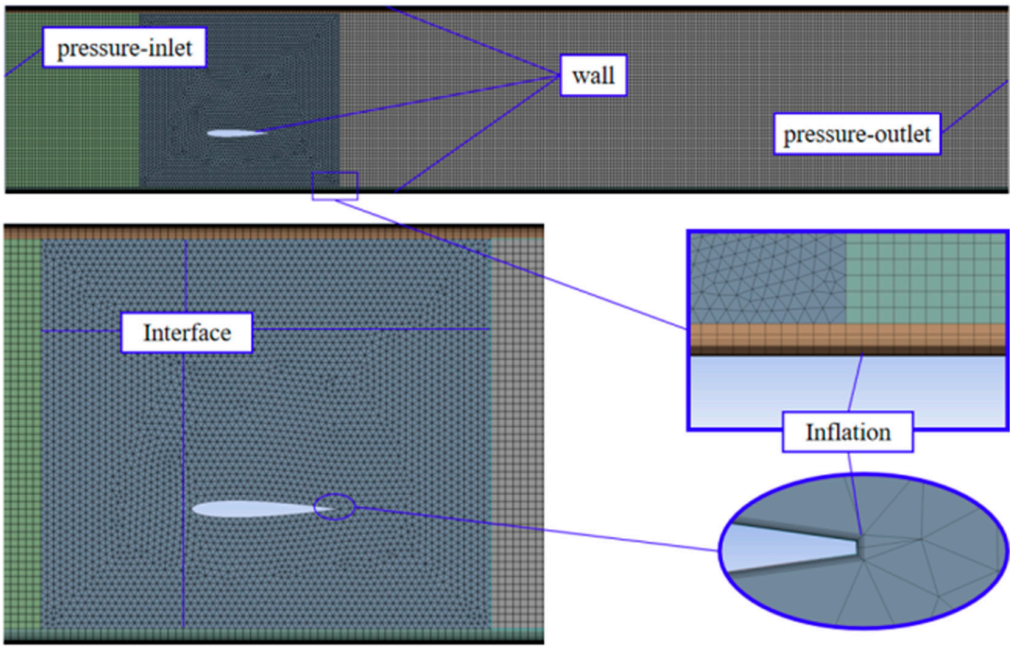

Figure 6. Schematic diagram of the computational domain.

2.3.2. Grid Independence Verification

The number of grids and time steps significantly affect the accuracy and stability of the model during numerical calculations, and different grid sizes correspond to different time steps. Especially in bidirectional fluid–structure interaction, the computation time will increase exponentially. In this paper, the commercial software Ansys—Workbench 2024 R1 was used to couple the Transient Structural module with the Fluent module through System Coupling, and a dual AMD EPYC 7542 32-Core processor was used in the calculations with 256 G of running memory. It was essential to guarantee the hydrodynamic parameters, such as the thrust and lift coefficient, in the Fluent calculation within the fluid domain. Similarly, the Transient Structural calculation within the solid domain ensured the accuracy of deformation. To guarantee the precision of the model and the efficacy of the solution, this paper compared the instantaneous thrust of a flexible hydrofoil (Shore hardness D50, corresponding to a modulus of elasticity of 0.4 G·Pa and a density of 0.92 g/cm^3) with an outward oscillating motion at a frequency of 0.5 Hz employed in a steady flow field; and with the fluid domain mesh numbers set at 44,591, 111,595, and 234,895, respectively; and the solid domain mesh numbers at 106, 921, and 2295, respectively. To circumvent any additional discrepancies that might arise when the fluid domain was incorporated into the coupling calculation, the solid domain mesh was validated with a fixed fluid domain mesh number of 111,595. The comprehensive mesh independence verification outcomes are presented in Figure 7.

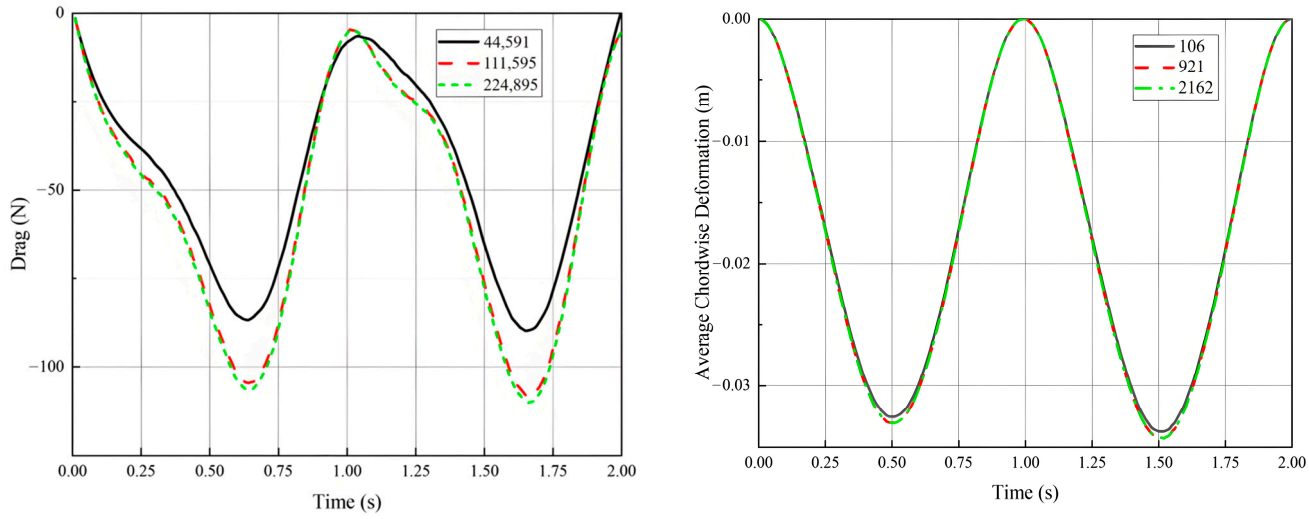

(**a**) (**b**)

Figure 7. Grid-independent verification: (**a**) Fluid domain mesh validation; (**b**) Solid domain mesh validation.

It is evident that the grid number 44,591 within the fluid domain resulted in a considerable discrepancy that failed to meet the prescribed computational standards. In contrast, a comparison of the calculations for the 110,000 grids and 230,000 grids revealed that the results of both calculations were essentially identical, and that the error would not have any impact on the conclusions of this study. However, the 110,000 grid number requires 34 h to calculate a single case, while the 230,000 grid requires 71 h, resulting in an exponential waste of computational resources. In the solid domain validation, the number of grids was found to have a negligible effect on the computational results. However, an average error of approximately 9.7% for chordal strains was observed at a grid number of 106. The computational results for 2162 grids were generally in agreement with the results obtained from the 921 grids, and with an average error of approximately 0.7%. However, the calculation time for a single case was 94 h longer for the 2162 mesh than for the 921 mesh. To conserve computational resources while maintaining the precision of the results, the initial grid number of 110,000 in the fluid domain and 921 in the solid domain was selected.

2.3.3. Validation of the Fluid–Solid Coupling Method

The bidirectional fluid–structure interaction method offered significant advantages over traditional dynamic meshing methods, enabling real-time feedback between the fluid forces and structural deformations to capture more accurate and realistic interactions in dynamic environments. This approach avoided the common limitations of dynamic meshing techniques, such as the inability to effectively deal with passive deformation in fluid mechanics. In fluid–solid coupling calculations, the fluid domain is coupled with the solid domain through a System Coupling module, a process that is inevitably accompanied by an increase in the potential for error and uncertainty. Heathcote, S. et al. [17] employed a water hole experiment to measure the change response of the thrust coefficient with heaving amplitude for three groups of airfoils, subsequently verifying the reliability of the measured data. To guarantee the dependability of the bidirectional fluid–structure interaction method presented in this paper, a model of the water hole experiment was constructed for the purpose of verifying the accuracy of the calculations presented in this paper. This is illustrated in Figure 8.

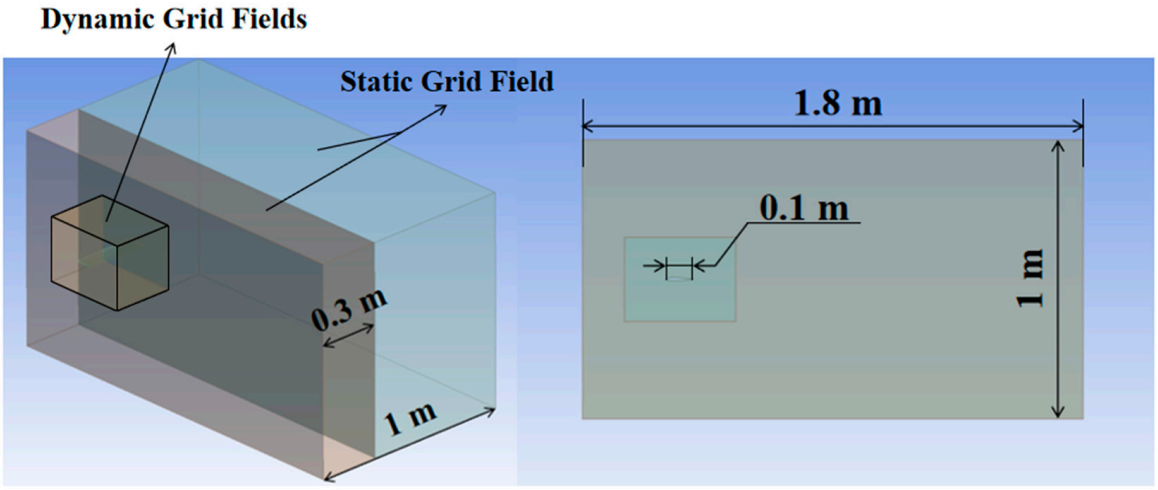

Figure 8. Modeling of the validation methods.

To evaluate the efficacy of the methodology presented in this paper, two sets of experiments on rigid and flexible hydrofoils, as documented in the literature, were selected for comparison with the calculated values obtained through the proposed method. The comparison results are illustrated in Figure 9. In the calculation, the hydrofoil was a pure heaving single degree of freedom motion; the equation of motion is shown in Equation (3), with the heaving amplitude h_{max} = 0.175 m, the heaving phase difference φ_h = 0, and the frequency f = 2 Hz. The hydrofoil consisted of rectangular stainless-steel reinforcement with E = 200 G·Pa, ρ = 7800 kg/m^3, and DPMS rubber with E = 2.5 × 10^{-4} G·Pa, ρ = 970 kg/m^3, the length of the flow channel at 1.8 m, and the height and width at 1 m.

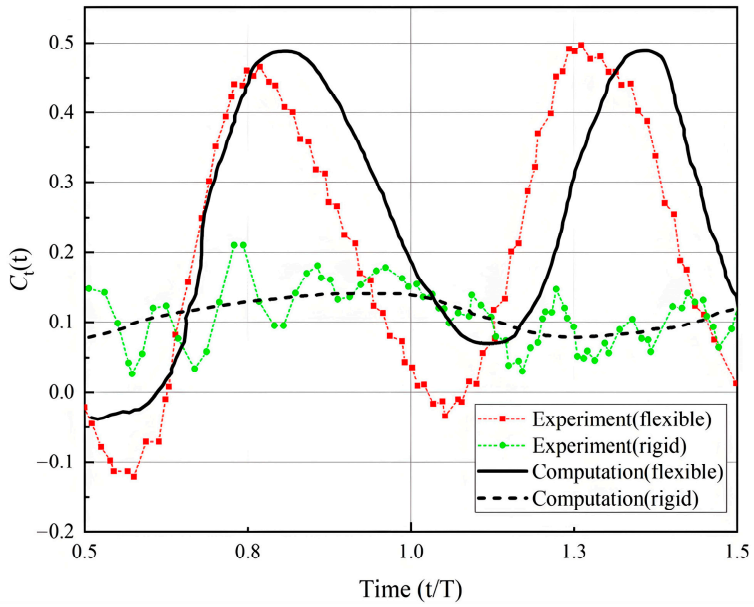

Figure 9. Comparison of test results with calculated results.

A comparison of the above results revealed that the numerical calculations of flexible hydrofoils were consistent with the experimental trend, with an insignificant error remaining after the neglect of time phase error had been eliminated. In contrast, the numerical calculations of the rigid hydrofoils exhibited relatively larger errors. This discrepancy may be attributed to the substantial vibration of the rigid hydrofoil during its movement within the water hole test, which resulted in considerable signal interference. The comparison results demonstrated that the trend of the thrust coefficient's change with time is

essentially consistent. However, the numerical calculation of the rigid hydrofoil effectively circumvented the signal interference caused by the transmission shaft or its own frequency resonance. This aligned more closely with the requisite calculation accuracy for this study, particularly in comparison to the experimental measurements. Considering the analyses, it can be concluded that the numerical calculation method proposed in this paper met the requisite standards of accuracy and effectiveness.

3. Results

3.1. Hardness Effects on Hydrofoil Hydrodynamic Characteristics

The deformation of a flexible hydrofoil in a water flow not only affects the thrust and lift of the hydrofoil but also has an impact on its pumping efficiency and propulsion efficiency. To gain a deeper understanding of these effects, the hydrodynamic performance of flexible hydrofoils under different strain conditions was simulated based on the fluid–solid coupling model. In this paper, we classified the hydrofoil materials into D10, D30, D50, D60, and D70 according to the Shore hardness, because for the materials, in the context of bidirectional fluid–structure interaction, the Shore hardness does not provide a direct definition, necessitating a classification system. The corresponding material data were selected for parameter mapping in this study based on the Shore hardness data from the Springer Material Data Handbook [18], as illustrated in Table 1. By comparing the hydrodynamic properties of hydrofoils with varying Shore hardnesses, a more rational hydrofoil material selection could be evaluated.

Table 1. Parametric mapping of hydrofoil materials. Silicone rubber (SiR), thermoplastic polyurethane elastomer (TPU), low-density Polyethylene (LDPE), ultrahigh-molecular-weight polyethylene (UHMWPE), and polypropylene (PP).

Hardness	D10	D30	D50	D60	D70
Mapping material	SiR	TPU	LDPE	UHMWPE	PP
Elastic Modulus (G·Pa)	0.005	0.015	0.4	0.7	1.3
Densities (g/cm^3)	1.1	1.1	0.92	0.93	0.9

As postulated by Zhang et al. [19], a minor chord-wise strain can effectively enhance the aerodynamic attributes of hydrofoils. In accordance with this, the chord-wise strain has the capacity to enhance the drag-to-lift ratio of hydrofoils, thereby exerting a beneficial influence on their hydrodynamic characteristics. To analyze the chord-wise strain of the hydrofoils of different materials and its relationship with hydrodynamic characteristics, this paper compared the average chord-wise strain (D_d) of the inward oscillation motion of hydrofoils under steady flow fields with different hydrofoil materials, as illustrated in Figure 10.

The results showed that the chord-wise strain of hydrofoils was basically inversely proportional to the hardness in a linear relationship. When the Shore hardness of the hydrofoil was D10, the chord-wise strain was the largest, 0.0349 m. When the Shore hardness was D70, the chord-wise strain was the smallest, 0.0089 m. To analyze the effect of the size of the chord-wise strain on the instantaneous thrust of the hydrofoils more clearly, this paper compared the instantaneous thrust change curves of the hydrofoils of five hardness materials in a single oscillation cycle in a steady flow field, as shown in Figure 11.

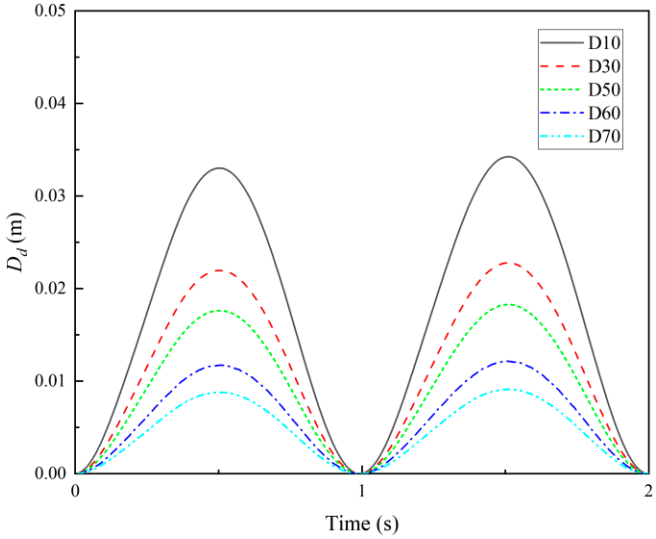

Figure 10. Hydrofoil chord-wise strain for five materials in a single kinematic cycle.

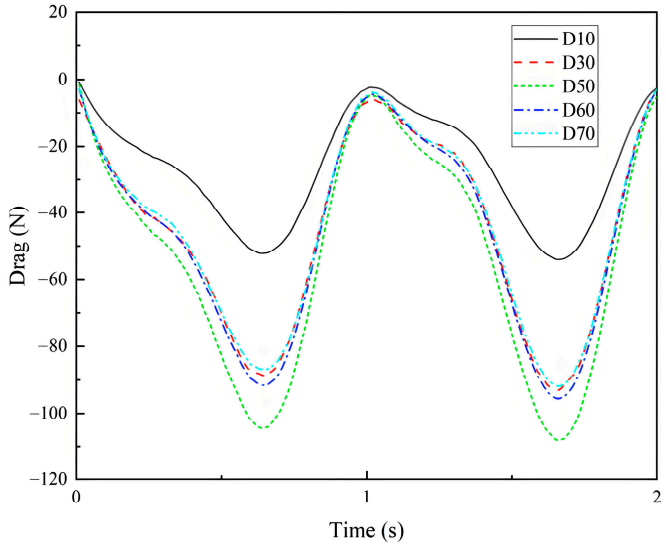

Figure 11. Transient thrust of hydrofoils at a single oscillation cycle of motion with five materials.

According to Figure 11, it can be seen that the hydrofoil obtained the largest peak instantaneous thrust at a Shore hardness of D50, which was 108.1 N; at a Shore hardness of D10, the peak instantaneous thrust of the hydrofoil was the smallest, which plummeted to 54.05 N; and at Shore hardness of D30, D60, and D70, the peak instantaneous thrusts were close to each other, which were 93.1, 95.6, and 91.9 N, respectively. It was obvious that the proper chord-wise deformation of the hydrofoil could have a favorable effect on the peak instantaneous thrust of the hydrofoil, but too much chord-wise deformation led to a decrease in the instantaneous thrust of the hydrofoil. This result is in some agreement with the study results of Zhang et al. [19]

In a recent study, Bilbao-Ludena et al. [20] conducted an analysis of the structure of vorticity and turbulence fields in the vicinity of a hydrofoil's surface utilizing direct numerical simulation (DNS). The researchers observed that the fluid separation resulted in the formation of a small reflux region in the vicinity of the wingtip, which exerted a significant influence on the generation and evolution of the vortices in this region. Similarly, the flow field around the flexible hydrofoil was investigated in this study. The results demonstrated that the distribution of the vortices and the characteristics of the flow field had a significant impact on the performance of the hydrofoil. As illustrated in Figure 12, the

generation of chord-wise deformation by the hydrofoil resulted in the partial absorption of the trailing edge vortex during the process of shedding, due to the hydrofoil shear force. The appropriate chord-wise deformation had the effect of reducing the viscous drag. The process of vortex shedding was accompanied by a rise in the drag coefficient, which was a consequence of the strengthening of the central vortex of the trailing edge vortex following its shedding. This, in turn, led to an increase in the drag experienced by the hydrofoil during its motion, resulting in a rise in the peak instantaneous thrust.

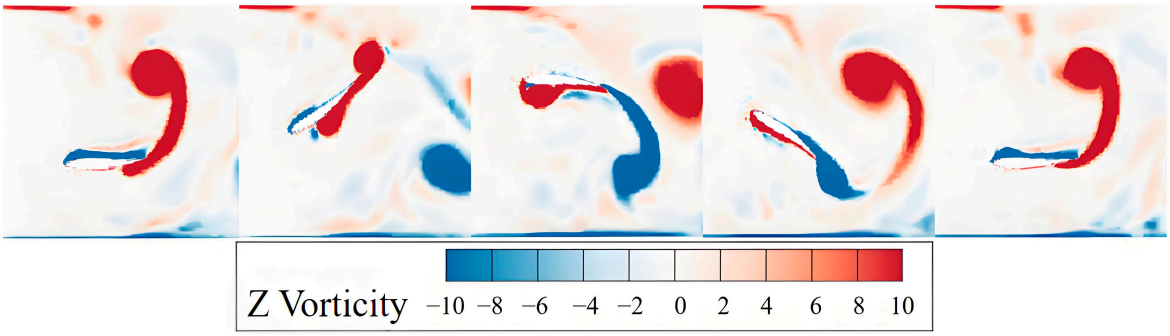

Figure 12. Trailing edge vortex shedding process.

To better assess the effect of hydrofoil hardness on the pumping efficiency, a comparative analysis of the hydrodynamic performance of hydrofoils with different Shore hardness D is also presented in this section. The analyses included drag-to-lift ratio, pumping efficiency, and propulsion efficiency as shown in Figure 13. The drag-to-lift ratio reflected the hydrodynamic performance of the hydrofoil during motion. A higher drag-to-lift ratio indicates that the hydrofoil can produce the same lift with less drag, which means less energy loss and higher efficiency. The results showed that the hydrodynamic performance of the hydrofoil was best when the Shore hardness was D50. When the Shore hardness exceeded D50, the drag-to-lift ratio, pumping efficiency, and propulsion efficiency of the hydrofoil gradually decreased as the hydrofoil hardness increased, resulting in a decrease in hydrodynamic performance. Conversely, when the Shore value was less than D50, the decrease in hydrofoil hardness resulted in a significant decrease in the drag-to-lift ratio and propulsion performance.

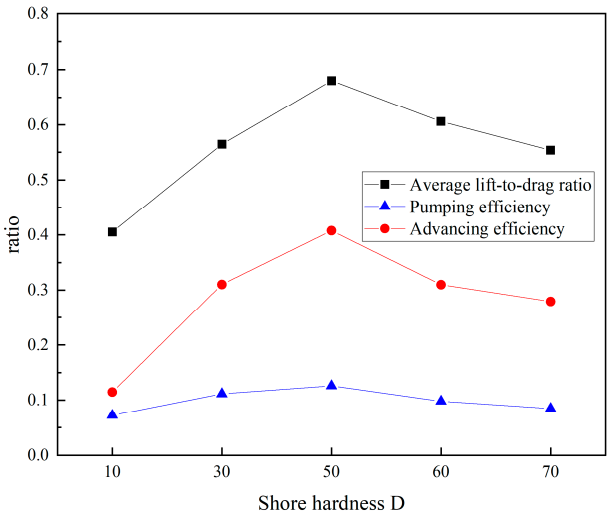

Figure 13. Comparison of hydrodynamic performance of hydrofoils of different stiffnesses under a single oscillation cycle.

Analysis of the results showed that the hydrofoil was capable of moderate deformation while maintaining a high degree of shape stability when its Shore hardness was D50. This increased the effective angle of attack and improved propulsion efficiency. A hydrofoil with excessive hardness was unable to adapt effectively to changes in hydrodynamic load, resulting in a reduction in the lift resistance ratio and a consequent deterioration in pumping and propulsion efficiency. Hydrofoils with insufficient hardness exhibited excessive deformation during oscillation, which resulted in partial energy loss and exacerbated tail vortex dissipation, thereby reducing the hydrodynamic performance of the hydrofoil. Furthermore, Figure 13 shows that the hardness of the hydrofoil had a pronounced effect on the propulsive efficiency, but a less pronounced effect on the pumping efficiency. This was mainly since the pumping efficiency is mainly dependent on the pressure difference between the inlet and outlet of the runner. Consequently, the deformation caused by the blade movement had relatively little effect on this.

3.2. Motion Way Effects on Hydrofoil Hydrodynamic Characteristics

To investigate the effect of the motion way on the hydrodynamic characteristics of the flexible hydrofoil, the material of the flexible hydrofoil in this paper was defined as LDPE with a Shore hardness of D50, based on the results in section A. The pumping and propulsion efficiencies of the flexible hydrofoil and the rigid hydrofoil were compared under steady flow conditions, considering pitch-only motion, and lifting-and-pitching-coupled inward and outward motions, as shown in Figure 14. The results showed that among the three modes of motion of the flexible hydrofoil, the inward oscillation mode had the most favorable hydrodynamic characteristics, followed by the outward oscillation mode. In contrast, the pitch-only oscillation motion mode had the least favorable hydrodynamic characteristics. The pitch-only oscillation motion resulted in a significant reduction in the propulsion and pumping efficiency of the flexible hydrofoil. On the contrary, the pitch-only oscillation motion of the rigid hydrofoil was superior to the outward oscillation motion under the same conditions. This result was consistent with the previous findings of Hua et al. [21]. Further, this paper discussed and analyzed the differences between the motion modes of flexible hydrofoils and their hydrodynamic performance compared to rigid hydrofoils.

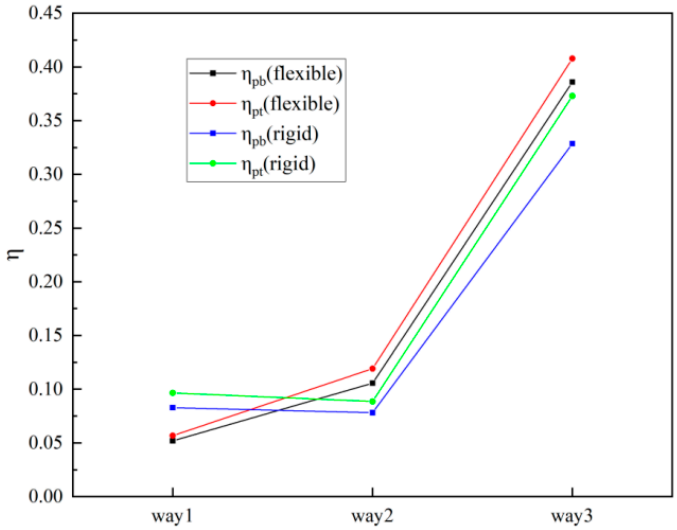

Figure 14. Comparison of pumping efficiency and propulsion efficiency between rigid and flexible hydrofoils with different oscillation modes.

To gain a more intuitive understanding of the hydrodynamic performance of the hydrofoils in three modes of oscillation, this paper presented a comparative analysis of the vortex structures and velocity distributions of the flexible hydrofoils in different modes of oscillation in a steady flow field. Figure 15 illustrates the vortex nephograms of the three modes in the steady flow field. From the vortex nephograms, it was observed that the trailing edge vortex center strength was higher in the inward oscillating motion mode, the stability of the reverse Kármán vortex street was higher, and the maximum dissipation distance was farther. This was followed by the outward oscillating motion mode, in which the reverse Kármán vortex street dissipated more quickly, and the vortex strength was relatively low. A comparison of the structures of the vortex street in the three modes of motion revealed that in the inward oscillation motion, the distance between the positive vortex and the negative vortex was relatively large in the Y-direction. This made the vortex street more effective in inducing a relatively smooth jet in the X-direction. In contrast, the relatively compact reverse Kármán vortex consumed a greater quantity of kinetic energy in the Y-direction in the pitch-only oscillation motion mode. This was due to the negative angle-of-attack condition of the hydrofoil during the outward pendulum motion, which resulted in the trailing edge vortex being pulled obliquely by the reverse force during shedding. This in turn weakened the strength of the center vortex and the shedding vortex's traversing velocity, leading to a concentration of the vortex near the hydrofoils, which reduced the average flow rate.

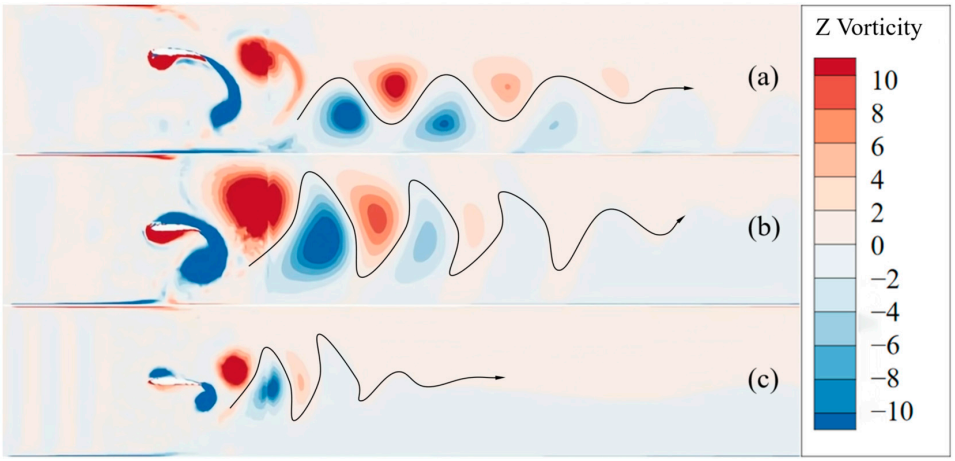

Figure 15. Comparison of the vortex nephograms of the flow field under different oscillation modes: (**a**) Inward oscillation mode. (**b**) Outward oscillation mode. (**c**) Pitch-only oscillation mode.

To show the change process of the surface vortex pattern during hydrofoil motion, this paper compared the changes in surface vortex between the rigid hydrofoil and flexible hydrofoil with the inboard oscillation motion and outer oscillation motion ways for a stable flow field in a single oscillation cycle. Figure 16 shows the comparison of the vortex structure between the rigid hydrofoil and flexible hydrofoil under the outer oscillation motion in a single cycle. When the trailing edge vortex was shed, the wingtip destroyed the integrity of the trailing edge vortex along the oblique direction, resulting in part of the trailing edge vortex being retained on the surface of the hydrofoil, which dissipated and generated additional drag during the reversed oscillations, consuming a large amount of the central vortex strength of the trailing edge vortex, and led to the rapid dissipation of the subsequently reversed Kármán vortex street. Comparing the vortex nephograms at the oscillation amplitude position, it was found that the flexible hydrofoil deformed due to inertial force at this position, exacerbating the negative angle-of-attack phenomenon, while the rigid wing just avoided the extra energy loss due to deformation. This phenomenon was more helpful in explaining the hydrodynamic difference between the rigid hydrofoil

and flexible hydrofoil in the outer oscillation and pitch-only oscillation modes as they appeared in Figure 14, which will be further analyzed in conjunction with the thrust curves and vortex nephogram later.

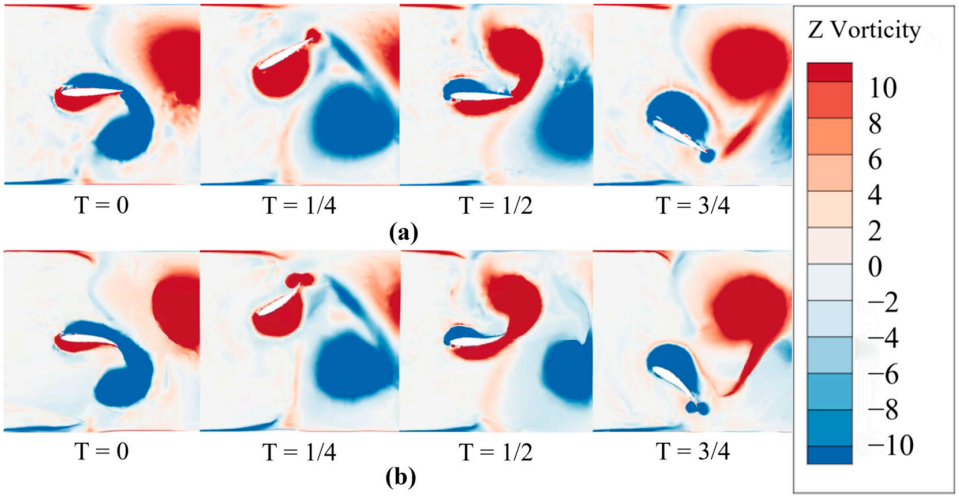

Figure 16. Comparison of the vortex structures on the surface of the rigid hydrofoil and the flexible hydrofoil under outward oscillating motion: (**a**) Rigid hydrofoil. (**b**) Flexible hydrofoil.

Figure 17 illustrates the vortex structures of the rigid and flexible hydrofoils in response to inward oscillation motion over the course of a single oscillation cycle. The analysis of the vortex structures indicated that the inward oscillation motion can result in the elongation of the shedding trailing edge vortex in a direction perpendicular to the incoming flow velocity. This resulted in the strengthening of the central vortex of the trailing edge vortex, an enhancement of the kinetic energy along the direction of the incoming flow velocity at the time of shedding, and a significant reduction in the dissipation speed of the vortex volume. In the case of the flexible hydrofoil, the chord-wise deformation of the hydrofoil reduced the surface resistance between the shedding vortex and the airfoil surface, increased the effective angle of attack of the hydrofoil, and was conducive to the enhancement of the trailing edge vortex strength. Conversely, the rigid hydrofoil was devoid of deformation at the wingtip, thereby retaining surface drag. This resulted in a reduction in hydrodynamic performance relative to the flexible hydrofoil.

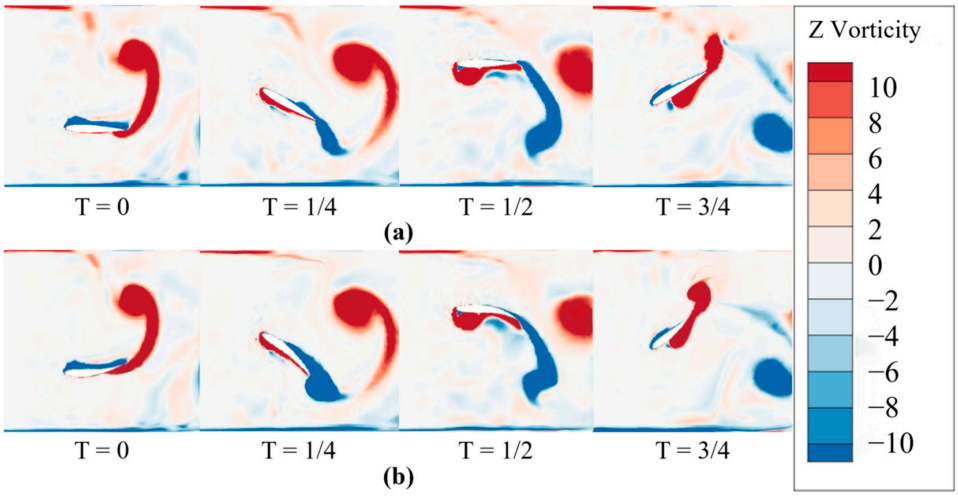

Figure 17. Comparison of the vortex structures on the surface between the rigid hydrofoil and the flexible hydrofoil under inward oscillating motion: (**a**) Rigid hydrofoil. (**b**) Flexible hydrofoil.

A more intuitive understanding of the force change of the hydrofoil during motion can be gained by linking the vortex structure change with the instantaneous thrust change. To illustrate, the flexible hydrofoil under consideration in this study exhibited distinct thrust curves in a single stable cycle across three distinct motion modes, as depicted in Figure 18. The results demonstrated that the flexible hydrofoil generated a heightened peak thrust under the outward oscillation motion, which can be attributed to the phenomenon of shed vortex stacking and squeezing. Near the wingtip, the outward oscillation motion gave rise to the accumulation of vortices at the trailing edge and the splitting of vortices at the wingtip, due to the deformation of the wingtip. This resulted in the consumption of additional kinetic energy during the reverse oscillation, which increased the instantaneous thrust of the hydrofoil, reduced the stability of the thrust curve, and consequently resulted in a significant efficiency loss. The pitch-only oscillation motion lacked the additional kinetic energy derived from the heaving motion. Furthermore, the thrust required to overcome the viscous drag on the hydrofoil surface during trailing edge vortex shedding was insufficient, resulting in the lowest instantaneous thrust. Furthermore, the maximum wing tip deformation at the flexible wing pitching amplitude position intensified the negative angle-of-attack issue due to the outward oscillation and pitch-only oscillation motions, which generated additional negative thrust. Conversely, the inward oscillation motion produced an additional effective angle of attack at the same position of the wing tip deformation, resulting in additional thrust while simultaneously enhancing the stability and flow field structure compared to the other oscillation modes.

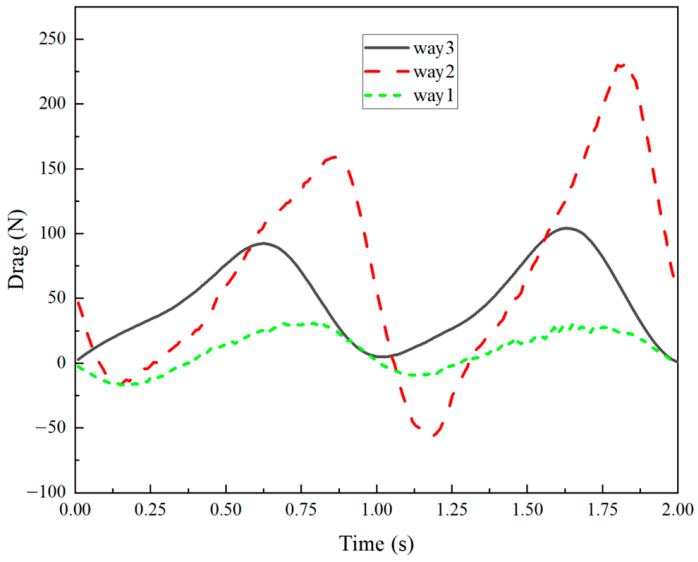

Figure 18. Instantaneous thrust curves for the three modes of hydrofoil motion in a single oscillation cycle.

The vortex effect [22] generated by the hydrofoil during its oscillation was a key factor in the generation of pumping or propulsion work. Additionally, the jet induced by the reversed Kármán vortex street generated during the motion was the main power source. This can be observed in conjunction with the analysis of the velocity nephogram of the flow field. Figure 19 illustrates the vortex nephogram of the flexible hydrofoil under the three oscillating modes. In the case of inward oscillation, the more uniform and lower dissipation rate-reversed Kármán vortex street could induce a jet that was both farther and more stable, thereby increasing the overall flow velocity. In the case of the outward oscillation and pitch-only oscillation motions, the latter was characterized by significant vortex depletion defects due to the insufficient strength of the vortex and the negative thrust exerted on the shedding vortex at the position of pitch amplitude. This resulted in

a notable reduction in the enhancement of the flow rate. While the outward oscillation motion exacerbated the energy loss at the pitching amplitude position due to the additional negative thrust brought about by the lifting-and-pitching motion, the results in Figure 14 indicated that this energy loss was offset by an ameliorating effect. A reduction in the hardness of the hydrofoils resulted in a differentiation of the hydrodynamic performance of rigid and flexible hydrofoils in pitch-only and outward oscillation motions.

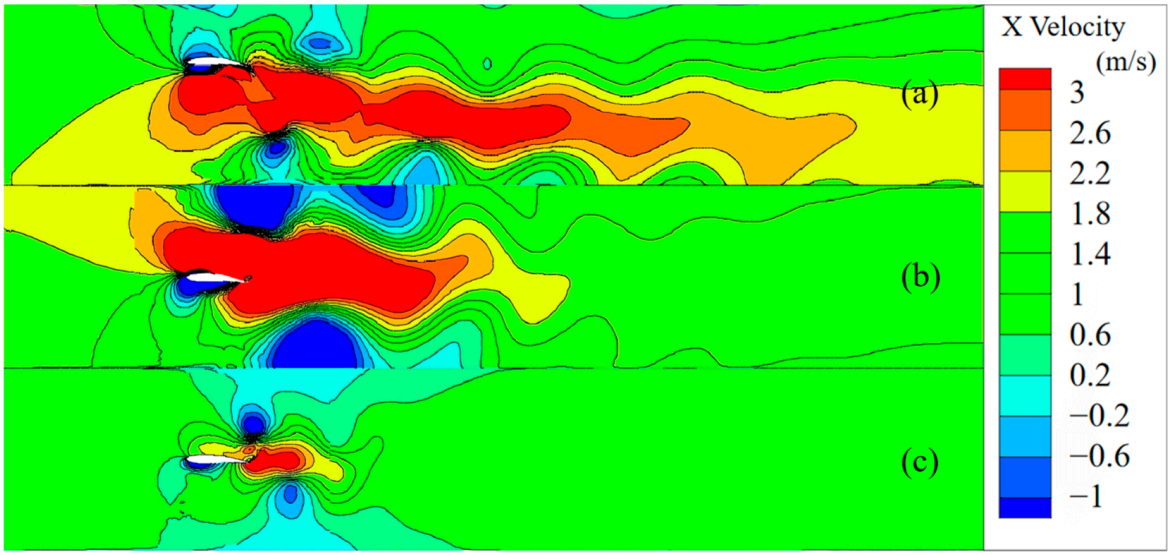

Figure 19. Comparison of the vortex nephograms of the flow field under different oscillation modes. (**a**) Outward oscillation. (**b**) Inward oscillation. (**c**) Pitch-only oscillation.

The inward oscillation propulsion method, when combined with the analyses, was found to significantly enhance the propulsion efficiency of the flexible hydrofoil, while also exhibiting superior hydrodynamic performance in practical applications. In terms of the three types of oscillation, inward oscillation was the most effective, outward oscillation was the second most effective, and pitch-only oscillation was the least effective. The hydrodynamic characteristics of the flexible hydrofoil were superior to those of the rigid hydrofoil under inward oscillation. Furthermore, the flexible hydrofoil expended additional kinetic energy because of the tail vortex splitting caused by the deformation of the wingtip and generated negative thrust due to the negative angle of attack. This led to a reduction in the hydrodynamic performance of the hydrofoil. In the case of outward oscillation, the presence of heaving motion generated additional negative thrust, which was further reduced when the hydrofoil hardness was slightly diminished. This resulted in the hydrodynamic performance of the flexible hydrofoil being superior to that of the rigid hydrofoil in the outward oscillation mode, while the converse was true in the pitch-only oscillation mode.

4. Conclusions

This paper investigated an existing flexible hydrofoil device that imitates the swimming characteristics of fish with a view to addressing the hydrodynamic insufficiency of ecological water bodies in the plains of southern China. The hydrodynamic characteristics of the NACA0012 two-dimensional flexible symmetric hydrofoil model with a chord length of c = 1 m under different hardnesses and oscillation modes were numerically simulated and analyzed by bidirectional fluid–structure interaction. The results demonstrated the superior hydrodynamic performance of the flexible hydrofoil under specific hardness and oscillation modes, and the primary conclusions are as follows:

- Among the five groups of hardness selected in this paper, the hydrofoils with a Shore hardness of D50 (e.g., LDPE) performed optimally in terms of propulsion efficiency, pumping efficiency, and drag-to-lift ratio. This level of hardness ensured good shape stability of the hydrofoil while allowing for proper chord-wise deformation, which optimized the effective angle of attack and drag-to-lift ratio and improved propulsion efficiency. Excessively high hydrofoil hardness could impede trailing edge vortex shedding, while excessively low hardness could cause additional energy loss and vortex dissipation, both of which led to reduced hydrodynamic performance. Hydrofoils with very low hardness experienced reduced force stability during pitch-only and outward oscillation motions, generating additional negative thrust, and further diminishing their overall hydrodynamic performance. The findings from the simulations clearly showed that a balanced Shore hardness (D50) provided optimal performance by enhancing the hydrofoil's ability to maintain shape stability and improve thrust generation.
- Among the three selected common motion ways, the inward oscillation motion way has the best performance among all the tested oscillation modes and had significant hydrodynamic improvement effects for both the rigid and flexible hydrofoils. For the inward oscillation motion way, the chord-wise deformation of the hydrofoil reduced the surface resistance between the shedding vortex and the hydrofoil surface and increased the effective angle of attack of the hydrofoil, which was conducive to the enhancement of the trailing edge vortex strength. The hydrodynamic performance of the flexible hydrofoil was better than that of the rigid hydrofoil in both outward oscillation and inward oscillation modes, while the hydrodynamic performance of the rigid hydrofoil was better than that of the flexible hydrofoil in the pitch-only oscillation mode.
- Combined with the comparative analysis of the vortex structure, velocity distribution of the flow field, and the observation of the instantaneous thrust curve, we found that the vortex structure formed by the inward oscillation motion way was more conducive to inducing a more distant and stable jet. For the inward oscillation motion way, the trailing edge vortex was elongated along the direction perpendicular to the incoming velocity, which enhanced the central vorticity of the trailing edge vortex, increased the kinetic energy along the direction of the incoming velocity when the trailing edge vortex was dislodged, and reduced the dissipation rate of the vortex substantially. In contrast, the outward oscillation and pitch-only oscillation motions led to rapid vortex dissipation due to the different direction of the force on the trailing edge vortex shedding, which affected the formation of the reversed Kármán vortex street and reduced the distance and stability of the jet, which in turn affected the overall hydrodynamic performance of the hydrofoil.

This study provided a systematic framework for optimizing the hydrodynamic performance of flexible hydrofoils, highlighting their significant advantages over rigid designs. The findings demonstrated that flexible hydrofoils with a Shore hardness of D50 and inward oscillation modes achieved superior efficiency and ecological compatibility, addressing critical challenges in water management. While this study focused on two-dimensional simulations, future research could explore three-dimensional effects, experimental validations, and the integration of active flexibility mechanisms to enhance adaptability. These efforts would further bridge the gap between theoretical advancements and real-world applications, promoting sustainable innovations in hydraulic and ecological engineering. In addition, this study was based on simulations conducted with constant Reynolds (Re) and Strouhal (St) numbers, reflecting specific flow conditions representative of ultra-low head applications. The choice of fixed Re and St numbers was also made to ensure the re-

producibility of the results, as it allowed for precise control over the simulation parameters and facilitated comparison with existing studies. While this approach enabled a focused analysis of the effects of Shore hardness and oscillation modes, it did limit the applicability of the findings to these specific flow conditions. Future work may explore a broader range of Re and St numbers to evaluate the performance and applicability of flexible hydrofoils under diverse flow regimes. Such an extension would provide a more comprehensive understanding of the hydrodynamic characteristics and enhance the versatility of the proposed solution.

Author Contributions: E.H. developed the main research methodology and experimental ideas; M.X. completed all experimental parts and finished writing the manuscript; Q.S. reviewed the manuscript and participated in revisions; T.W. participated in data post-processing and model debugging; Y.S. participated in model construction, simulation experiments, and validation; and C.L. provided ideas for writing and detail improvement. All authors have read and agreed to the published version of the manuscript.

Funding: This research was funded by the Zhejiang Provincial Key Research and Development Project (Grant No. 2021C03019).

Institutional Review Board Statement: Not applicable.

Informed Consent Statement: Not applicable.

Data Availability Statement: All data and models generated or used during this study appear within the submitted article.

Conflicts of Interest: The authors declare no conflicts of interest.

References

1. Jin, D.; Sun, Y.; Zhong, W. Analysis of influencing factors of water body mobility in southern river network regions. *Zhejiang Hydrotech.* **2013**, *41*, 36.
2. Dai, Q. Status quo and development direction of large low-lift pump installations. *Jiangsu Water Resour.* **2018**, *6*, 54.
3. Feng, Y.; Su, Y.; Su, Y.; Liu, H. Research on hydrodynamic performance of oscillating hydrofoils based on fish-like swimming patterns. *J. Huazhong Univ. Sci. Technol. (Nat. Sci. Ed.)* **2019**, *47*, 38.
4. Du, X.; Zhang, Z. Numerical analysis of the influence of four flapping modes on the performance of underwater flapping-wing propulsion. *Eng. Mech.* **2018**, *35*, 249.
5. Ding, H.; Song, B.; Tian, W. Analysis of underwater biomimetic flapping-wing propulsion performance. *J. Northwestern Polytech. Univ.* **2013**, *31*, 150.
6. Li, Y.; Wang, J.; Chen, J. Numerical simulation of flapping wing propulsion characteristics considering wall effects. *Nav. Archit. Ocean. Eng.* **2020**, *36*, 26.
7. Ryu, Y.; Chang, J.; Chung, J. Aerodynamic characteristics of flexible wings with leading-edge veins in pitch motions. *Aerosp. Sci. Technol.* **2019**, *86*, 558. [CrossRef]
8. Liu, P.; Liu, Y.; Huang, S.; Zhao, J.; Su, Y. Effects of regular waves on propulsion performance of flexible flapping foil. *Appl. Sci.* **2018**, *8*, 934. [CrossRef]
9. Zhou, K.; Liu, J.; Chen, W. Numerical study on hydrodynamic performance of bionic caudal fin. *Appl. Sci.* **2016**, *6*, 15. [CrossRef]
10. Wang, Z.; Zhang, X.; Cong, W. Study on the influence of chord-wise deformation mode of flexible flapping hydrofoil on propulsion performance. *J. Ship Mech.* **2010**, *14*, 699.
11. Gao, P.; Huang, Q.; Pan, G.; Zhao, J. Experimental study on hydrodynamic characteristics of flexible flapping hydrofoil. *J. Huazhong Univ. Sci. Technol. (Nat. Sci. Ed.)* **2022**, *50*, 144.
12. Deng, J.; Caulfield, C. Three-dimensional transition after wake deflection behind a flapping foil. *Phys. Rev. E* **2015**, *91*, 043017. [CrossRef]
13. Hua, E.T.; Su, Z.; Xie, R.; Chen, W.; Tang, S.; Luo, H. Optimization and experimental verification of pivot position of underwater flapping wing. *J. Hydroelectr. Eng.* **2023**, *42*, 128.
14. Shaheed, R.; Mohammadian, A.; Gildeh, H.K. Comparison of standard k-ε and realizable k-ε turbulence models in curved and confluent channels. *Environ. Fluid Mech.* **2019**, *19*, 543. [CrossRef]

15. Jiang, Y.; Wang, C.; Li, J.; Wang, C.; Wang, Q. Study on flow-induced vibration characteristics of 2-DOF hydrofoil based on fluid-structure coupling method. *J. Mar. Sci. Appl.* **2023**, *22*, 775. [CrossRef]
16. Qi, Z.; Jia, L.; Qin, Y.; Shi, J.; Zhai, J. Propulsion performance of the full-active flapping foil in time-varying freestream. *Appl. Sci.* **2020**, *10*, 6226. [CrossRef]
17. Heathcote, S.; Wang, Z.; Gursul, I. Effect of spanwise flexibility on flapping wing propulsion. *J. Fluids Struct.* **2008**, *24*, 183. [CrossRef]
18. Warlimont, H.; Martienssen, W. *Springer Handbook of Materials Data*; Springer: Cham, Switzerland, 2018; pp. 495–517.
19. Zhang, X.; Zhou, C.; Xie, P. Numerical study on the effect of flapping wing flexibility on hovering aerodynamic characteristics. *J. Harbin Inst. Technol.* **2012**, *44*, 115.
20. Bilbao-Ludena, J.; Papadakis, G. Structure of vorticity and turbulence fields in a separated flow around a finite wing: Analysis using direct numerical simulation. *Phys. Rev. Fluids* **2023**, *8*, 014704. [CrossRef]
21. Hua, E.T.; Tang, S.; Chen, W.; Xie, R.; Guo, X. Influence of flapping mode of oscillating hydrofoil on water propulsion. *J. Hydroelectr. Eng.* **2022**, *41*, 93.
22. Daghooghi, M.; Borazjani, I. The hydrodynamic advantages of synchronized swimming in a rectangular pattern. *Bioinspiration Biomim.* **2015**, *10*, 056018. [CrossRef]